Bi-Directional Energy Cascades in the Pacific Ocean From Equator to Subarctic Gyre

Bo Qiu, Toshiya Nakano, Shuiming Chen, Patrice Klein

Bi-directional Energy Cascades in the Pacific Ocean from Equator to Subarctic Gyre

Bo Qiu[1], Toshiya Nakano[2], Shuiming Chen[1], Patrice Klein[3,4]

[1]Department of Oceanography, University of Hawaii at Manoa, Honolulu, Hawaii, USA

[2]Atmosphere and Ocean Department, Japan Meteorological Agency, Tokyo, Japan

[3]Environmental Science & Engineering, California Institute of Technology, Pasadena, CA, USA

[4]Jet Propulsion Laboratory, California Institute of Technology, Pasadena, CA, USA

Corresponding author: Bo Qiu: bo@soest.hawaii.edu

Key Points:

- Nonlinear interaction in upper ocean transfers kinetic energy both up- and down-scales
- Upper ocean balance and unbalanced motions contribute oppositely to energy cascade
- Bi-directional energy cascade depends on relative importance of balanced vs. unbalanced motions and characteristics of the unbalanced motions

This article has been accepted for publication and undergone full peer review but has not been through the copyediting, typesetting, pagination and proofreading process, which may lead to differences between this version and the Version of Record. Please cite this article as doi: 10.1029/2022GL097713.

Abstract

Ocean circulation receives its energy input at basin scales while dissipates at microscopic mixing scale. How this energy is transferred across different lengthscales is of paramount importance for understanding the ocean circulation equilibration and variability. Advancement in high-resolution numerical simulations in recent years has significantly improved our understanding of kinetic energy cascades from basin to kilometer scales, although observational evidence to verify the simulated processes remains limited. Using repeat ship-board velocity measurements along 165°E across the equatorial, subtropical and subarctic Pacific Ocean, we show that the length scale separating the inverse and forward cascades, L_S, falls in the 8~300km range and it does not scale straightforwardly with the baroclinic deformation radius. Balanced and unbalanced oceanic motions co-exist in this range but contribute oppositely to the directional energy cascades. L_S is observed to depend on the relative strengths of these motions, as well as by their interaction.

Plain Language Summary

This paper investigates how nonlinear interactions in the turbulent upper ocean transport kinetic energy (KE) across different spatial scales. This investigation is important because the energy input that drives the ocean circulation has scales at tens of thousand kilometers, whereas the oceanic mixing and dissipation take place below the centimeter scales. How oceanic KE is transported from one scale to another is neither fully understood nor adequately observed, and this is particularly true in the oceanic meso-submesoscales in the 1~300 km range. By using repeat shipboard Acoustic Doppler Current Profiler (ADCP) surveys from 2004 to 2020 in the western Pacific Ocean, we examined the cross-scale KE transfers in dynamically-different regimes of tropics, subtropics and high latitudes. We found that the KE can transfer both up-scales and down-scales due to the co-existence of balanced geostrophic motions and unbalanced wave motions. The length scale that separates the bi-directional KE transfers is geographically-dependent. It is controlled by the relative strengths of co-existing balanced and unbalanced motions, as well as by how the unbalanced wave motions are dynamically generated.

1 Introduction

Oceanic motions are multi-scaled, ranging from wind-driven gyre scales set by basin geometry to turbulent mixing scale of a few centimeters. As the energy source supplied by atmosphere is of basin scales, the induced oceanic motion needs to transfer the energy down-scales so that it could be dissipated at mixing scales and a global circulation equilibration could be reached (Ferrari and Wunsch 2009). Due to the Earth rotation and stratification, oceanic motions with different spatial scales are subject to different dynamical constraints. At basin scales, surface wind- and buoyancy-driven circulation is dictated by planetary geostrophic dynamics and theoretical framework, such as the ventilated thermocline theory, is well established. Energy transfer from the basin-scale circulation to mesoscales of O(10^2~10^3km) takes place due to baroclinic/barotropic instabilities. The Rossby number associated with the mesoscale instabilities is often small and the quasi-geostrophic (QG) dynamics forms a solid foundation to describe their properties and evolution.

Our understanding about the oceanic mesoscale variability and interaction have improved significantly following the advent of satellite altimetry measurements (Fu et al. 2010). Using gridded sea surface height (SSH) data, Scott and Wang (2005) presented evidence that kinetic energy (KE) transfer in the surface ocean is bi-directional, cascading up-scales at large lengthscales and down-scales at small lengthscales. The separation scale, L_S, between the inverse and forward cascade is found to be latitude-dependent; in the South Pacific, for example, L_S = 250~300km in 10°-20°S and 120~150km in 50°-60°S. Following their analysis, many observational and modeling studies have confirmed the inverse cascade in the global surface ocean and L_S has often been identified as the energy injection scale corresponding to the maximum instability of larger-scale circulation (Schlösser and Eden 2007; Qiu et al. 2008; Aluie et al. 2018). Although not exactly proportional to the baroclinic deformation radius L_D, there is a consensus based on satellite altimetry data that L_S is related to L_D and that it shortens from ~300km in tropics to ~150km in high-latitude oceans (Tulloch et al. 2011; Arbic et al. 2013; Wang et al. 2015).

Given the 100~300km spacing between satellite groundtracks, the presently-available 2-dimensional SSH dataset has a spatial resolution on the order of 150km (Chelton et al. 2011). This observational capability prevents us from detecting smaller mesoscale features and misses completely the important submesoscale processes that lie below L_D down to the km scale. Indeed, many recent high-resolution simulations reveal that the inverse cascade in the upper ocean can be found at lengthscales an order-of-magnitude smaller than those inferred from the altimetric data (Capet et al. 2008; Klein et al. 2008; Qiu et al. 2014; Sasaki et al. 2014). In other words, the simulated L_S falls in the submesoscale range where Rossby and Froude numbers are O(1). One energy source for the submesoscale upper ocean variability is surface mixed layer instability which draws available potential energy from laterally-stratified mixed layer (Boccaletti et al. 2007; Fox-Kemper et al. 2008) and the inverse KE cascade in this case can be understood in the framework of surface QG dynamics (Held et al. 1995).

While our understanding about the cross-scale interaction down to submesoscales has increased significantly from high-resolution numerical simulations, direct ocean measurements that can be used to verify this interaction remain limited. Densely-deployed surface drifter measurements have been used recently to explore the scale interaction across the submesoscale range. In the Gulf of Mexico, analyses of drifter-derived velocity structure function reveal that the separation scale from inverse to forward cascades occurs near L_S =5km (Balwada et al. 2016; Poje et al. 2017).

Shipboard Acoustic Doppler Current Profiler (ADCP) measurements are another effective tool to observe the upper ocean velocities down to submesoscales. With research vessels sailing at a speed of ~5m/sec, the ADCP velocity signals have a spatial resolution of 1~2 kilometers. Many investigators have in the past utilized the ADCP data to separate balanced flows from unbalanced motions and explored their relative contributions to the KE wavenumber spectra at different oceanic regions (Callies and Ferrari 2013; Callies et al. 2015; Rocha et al. 2016; Qiu et al. 2017; Chereskin et al. 2019; Sérazin et al. 2020). A consensus resulting from these studies is that the balanced flows in the meso-submesoscale range has a KE spectral slope of k^{-2}~k^{-3} as a result of interior and surface-intensified baroclinic instability, where k is horizontal wavenumber. As lengthscale shortens, velocity signals tend to be taken over by unbalanced motions with shallower spectral slopes. The transition scale from dominance by balanced to unbalanced motions depends on the KE levels of balanced vs. unbalanced motions and it is typically <50km in the western boundary current and Antarctic Circumpolar Current regions, ~100km in the subtropical countercurrent regions, and >200km in the tropics and regions of weak mesoscale variability across the global ocean.

The past ADCP analyses have focused on the spectral characteristics of upper ocean velocities. The objective of our present study is to go beyond this characterization and to explore the scale interaction in the oceanic meso-submesoscale range. Theoretically, while the quasi two-dimensional balanced flow variability favors inverse cascade, unbalanced motions interact to contribute to forward cascade. The goal of our study is to evaluate the scale L_S that separates the inverse cascade from forward cascade in different oceanic regimes. To achieve this, we analyze the repeat shipboard ADCP surveys conducted by Japan Meteorological Agency (JMA) along 165°E in the past two decades. As shown in Fig.1a, the 165°E section traverses from 5°S to 50°N in the western Pacific Ocean and encompasses five bands in which the background circulation and eddy variability exhibit dynamically distinct characteristics. By examining the second- and third-order velocity structure functions in each of these bands, we quantify how L_S varies and elucidate the processes responsible for the different L_S values.

2 ADCP data

Repeat hydrographic and shipboard ADCP surveys have been conducted by JMA along 165°E using dedicated research vessels (Nakano et al. 2018). We selected a total of 38 available transects from 2004 to 2020 for analysis in this study. Among these transects, 13 covered

northern segment north of ~30°N and the remaining transects covered the southern segment (Fig.1b). Seasonally, all northern cruises were occupied in summer, while the southern cruises had a mixture of winter and summer occupations. As in previous studies utilizing the shipboard ADCP data, we assume that the ship velocity, averaged at 5m/sec, is faster than the evolving meso-submesoscale features of our interest. The processed ADCP data are averaged in 5-min (~2.2km) horizontal and 16~20-m vertical bins. Further information about the ADCP data can be found in Supporting Information A.

3 Velocity structure function analysis

In each oceanic band, we first subtract the transverse (u_T) and longitudinal (u_L) velocities from their time-mean values from available cruises (see Fig.2a for the time-mean u_T profile). From u_T' and u_L', the second-order structure functions (SFs) for the longitudinal and transverse velocities are given by:

$$D2_L(r) = \langle \delta u_L^2(r) \rangle, \quad D2_T(r) = \langle \delta u_T^2(r) \rangle, \tag{1}$$

where r denotes the separation distance along the cruise track, $\delta u_T(r) = u_T'(y) - u_T'(y+r)$, $\delta u_L(r) = u_L'(y) - u_L'(y+r)$, and $\langle\ \rangle$ denote ensemble average over all y points within the band under consideration. For homogeneous and isotropic turbulent flows, second-order SF is related to the KE spectrum $E(k)$ through (Davidson 2015):

$$D2(r) = 4\int_0^\infty E(k)[1 - J_0(kr)]dk, \tag{2}$$

where $J_0(kr)$ is the zeroth-order Bessel function and k is horizontal wavenumber. If $E(k)$ decreases as k^{-m} with 1< m < 3, $D2(r)$ would increase proportional to r^{m-1} (Lindborg 2007). An $E(k)\sim k^{-5/3}$ scaling for 3-dimensional turbulent flow, for example, results in $D2(r)\sim r^{2/3}$, an $E(k)\sim k^{-3}$ scaling for quasi-geostrophic turbulent flow leads to $D2(r)\sim r^2$, and an $E(k)\sim k^{-2}$ scaling for submesoscale frontal turbulence produces $D2(r)\sim r$.

Helmholtz decomposition can be used to separate the along-track horizontal velocity into its rotational and divergent motions (Bühler et al. 2014). Under the assumption that they are uncorrelated, the second-order SF for the rotational and divergent velocity components, $D2_R(r)$ and $D2_D(r)$, can be derived from $D2_L(r)$ and $D2_T(r)$ via (Lindborg 2015):

$$D2_R(r) = D2_T(r) + \int_0^r \frac{1}{r}(D2_T - D2_L)dr,$$

$$D2_D(r) = D2_L(r) - \int_0^r \frac{1}{r}(D2_T - D2_L)dr. \tag{3}$$

Notice that for $D2_T(r)\sim D2_L(r)\sim r^m$, Eq.(3) indicates a pure rotational flow with $D2_D = 0$ should have $D2_T/D2_L = m + 1$.

The third-order velocity SF is related to the directional spectral energy or enstrophy fluxes (Lindborg and Cho 2001). For an isotropic and steady-state 3-dimensional turbulent flow under

forward KE cascade, the third-order longitudinal velocity SF is related to the energy dissipation rate ε by Kolmogorov's 4/5-law: $\langle \delta u_L^3(r) \rangle = -\left(\frac{4}{5}\right)\varepsilon r$. In regard to the energy cascade in 2-dimensional turbulence, the third-order SF can be expressed as:

$$D3_L(r) = \langle \delta u_L(r)[\delta u_L^2(r) + \delta u_T^2(r)] \rangle = -2Fr, \quad (4)$$

where $\boldsymbol{F}$ is sign sensitive. If $\boldsymbol{F} > \boldsymbol{0}$, it implies a forward cascade with $\boldsymbol{F} = \boldsymbol{\varepsilon}$. An inverse cascade is implied if $\boldsymbol{F} < \boldsymbol{0}$. Notice that for both 2- and 3-dimensional turbulence, $\boldsymbol{D3_L(r) < 0}$ is indicative of a downscale KE cascade.

4 Results

Oceanic circulation along 165°E can be divided into five bands with distinct governing dynamics and turbulent characteristics: the Western Subarctic Gyre (WSG) band, the Kuroshio Extension band, the Subtropical Countercurrent (STCC) band, the North Equatorial Current (NEC) band, and the equatorial band (Fig.2). Details about the background circulation in each of these five bands are provided in Supplementary Information B. To ensure the spatial homogeneity upon which the SF analysis relies, we conduct our analyses using the ADCP data in these five bands separately. The SF results presented in this section are based on velocities averaged in the 40-100m upper ocean.

4.1 The Kuroshio Extension band (30°–40°N)

Figure 3c (solid blue and red lines) shows $D2_L(r)$ and $D2_T(r)$ as a function of r. For $r = 5{\sim}100$km, $D2_L(r)$ and $D2_T(r)$ are both proportional to $r^{1.6}$, indicating the variability in this range is dictated by a mixture of QG instability ($\sim r^2$) and submesoscale frontal instability ($\sim r^1$). This result is consistent with the findings by high-resolution numerical simulations that show the upper ocean Kuroshio Extension variability stems from combined QG baroclinic instability and surface-intensified mixed layer instability (Sasaki et al. 2014; Qiu et al. 2018). The dominance of velocity fluctuations by the instability-induced rotational motions can be further confirmed when we decompose the observed velocity into its rotational and divergent components. As shown by dashed red and blue lines in Fig.3c, the second-order SF $D2_R(r)$ is at least 5 times great than $D2_D(r)$ when $r > 10$km.

Figure 3d shows the third-order SF, $D3_L(r)$, in the Kuroshio Extension band. In the range $r = 2.5{\sim}150$ km, $D3_L(r)$ scales roughly with r^1, suggesting an inertial range energy cascade. Specifically, a forward cascade, or $D3_L(r) < 0$, occurs at $r \leq 5$km. For $r > 8$km, $D3_L(r) > 0$ and an inverse cascade with KE transferred up-scales is indicated. The relatively short separation scale of $L_s = 8$km and the dominance of inverse cascade in the Kuroshio Extension band are consistent with the Fig.3c result that the rotational velocities associated balanced motions overwhelm the divergent velocities by unbalanced motions in this band.

4.2 The STCC band (17°–30°N)

STCC has similar governing dynamics as the Kuroshio Extension although its eddy variability has a smaller amplitude due to weak baroclinicity. Reflecting this difference, Fig.3e shows that $D2_L(r)$ and $D2_T(r)$ have shallower slopes proportional to $r^{1.0}$ at $r = 10{\sim}100$km. This implies the regional meso-submesoscale variability is controlled more by the shallow frontal instability than by the interior QG instability. Compared to the Kuroshio Extension band, the difference between $D2_R(r)$ and $D2_D(r)$ is reduced across all resolved r values in Fig.3e than in Fig.3c. This reduced difference is both because the weaker balanced variability in this band and because the elevated unbalanced motions due to the presence of Mariana Ridges along 142°E and 146°E that provides a source for internal tide and inertia-gravity wave generations (Zhao and D'Asaro 2011).

Similar to the Kuroshio Extension band, $D3_L(r)$ in the STCC band increases roughly with r^1 in the $r = 2.5{\sim}150$km range, indicating again an inertial range energy cascade. Compared to the Kuroshio Extension band, the scale separating forward from inverse cascade increases to L_S = 15km (Fig.3f). The broadening of the forward cascade, or the $D3_L(r) < 0$ range, is due to the reduction (enhancement) in balanced (unbalanced) motion in the STCC band. Another interesting feature revealed in Fig.3f is that $D3_L(r)$ switches from positive to negative when r exceeds 300km. Such a feature where an inverse KE cascade reverses to a forward cascade when lengthscale increases, is also found by Klein et al. (2008; their Fig.11b) in their high-resolution model simulation that explored a re-entrant turbulent baroclinic jet. Dynamically, this occurs because while the balanced motion works to generate upscale spectral KE fluxes, scale-dependent covariance between the divergent flow and eddy kinetic energy can force the spectral KE flux by combined balanced+unbalanced motions in a downscale direction.

4.3 The Equatorial band (5°S–7°N)

Figures 1a and 2b reveal that the surface ocean eddy variability level in the equatorial band falls between the Kuroshio Extension and STCC bands. Despite this level of high eddy activity, SFs in the equatorial band have characteristics very different from the latter two bands. At $r <$ 20km, Fig.3i shows that $D2_L(r)$ and $D2_T(r)$ have equal amplitudes and this leads to equal amplitudes for $D2_R(r)$ and $D2_D(r)$ according to Eq.(3). As r lengthens from 20 to 200km, the $D2_R(r)/D2_D(r)$ ratio increases progressively, revealing the gradual dominance by balanced motion relative to unbalanced motion. When $r > 200$km, $D2_R(r)/D2_D(r)$ exceeds O(10), indicating the control by balanced motion at scales larger than the local deformation radius. Evaluation of $D3_L(r)$ reveals that forward KE cascade occupies a wide range of r in the equatorial band and it is only when the flow becomes fully rotational at $r > 200$km does the KE cascade reverses from downscale to upscale (Fig.3j). From the slope in the $r < 200$ km range of Fig.3j, the KE dissipation rate $\varepsilon = -D3_L(r)/2r$ is estimated to be $0.3\text{x}10^{-8}$ m^2/s^3. This inferred ε rate is consistent with the dissipation rate based on microstructure measurements in the western equatorial Pacific Ocean (Richards et al. 2015).

4.4 The NEC band (7°–17°N)

Different from the equatorial band, the off-equatorial NEC band has a low eddy activity level. The second-order SFs in this band, nevertheless, share many features similar to the equatorial band. For example, $D2_R(r)$ and $D2_D(r)$ have equal amplitudes at $r < 10$km and the $D2_R(r)/D2_D(r)$ ratio increases progressively as r lengthens from 10 to 100km (Fig.3g). As r exceeds 100km, $D2_R(r)$ becomes an order-of-manitude greater than $D2_D(r)$ and the flow turns predominantly rotational. Notice that because the flow field in this band is so depleted of the balanced eddy variability, $D3_L(r)$ remains negative until r reaches 300km (Fig.3h). That the separation scale L_S in both the NEC and equatorial bands of the western tropical Pacific is on the order of 200~300km, is consistent with the high-resolution regional model study by Zedler et al. (2019). In terms of the dissipation rate in the forward cascade range, the NEC band has an inferred $\varepsilon = 0.3\text{x}10^{-8}$ m^2/s^3 rate similar to the equatorial band.

4.5 The WSG band (40°–50°N)

The Western Subarctic Gyre has the lowest eddy variability level along the 165°E section. At $\boldsymbol{r < 25}$km in this band, $\boldsymbol{D2_R(r)}$ has a smaller amplitude than $\boldsymbol{D2_D(r)}$ (Fig.3a). Even when $\boldsymbol{r}$ increases, the $\boldsymbol{D2_R(r)/D2_D(r)}$ ratio remains <5 in this high-latitude band and this ratio is the smallest among the five bands analyzed in this study. Both the weak balanced eddy activity and enhanced unbalanced motions contribute to this small ratio. It is worth noting the unbalanced motions in the WSG band are induced by wind-forced near-inertial motion (Chaigneau et al. 2008; Alford et al. 2016). This is in contrast to the lower latitude bands where the unbalanced motions are largely induced by internal tides (Richman et al. 2012; Savage et al. 2017). An interesting result in this band is that rather than having a forward cascade over a broad $\boldsymbol{r}$ range, $\boldsymbol{D3_L(r)}$ is in fact positive and scales roughly with $\boldsymbol{r^1}$ in the $\boldsymbol{r = 10\sim50}$km range. Possible cause for this narrow-windowed inverse cascade will be commented on below in discussion.

5 Discussion

By analyzing the shipboard ADCP data along 165°E from 2004–2020, we have explored the turbulent characteristics and bi-directional KE cascades across the western Pacific Ocean. Co-existence of balanced and unbalanced motions is found to play an important role in affecting the direction of KE cascade. Specifically, the separation scale L_S that divides forward from inverse cascade is found to be controlled by the relative amplitudes of balanced and unbalanced motions, the nature of the unbalanced motions, and the regional baroclinic deformation radius. This finding is in contrast to the analyses based on satellite altimeter data which suggested L_S could be scaled by the baroclinic deformation radius. This contrast stems from the fact that altimeter SSH measurements capture the balanced upper ocean variability *only* whose nonlinear interaction favors inverse KE cascade. The spatial resolution of >100km by the altimeter-gridded SSH field also imposes a restriction on accurately capturing the L_S value.

As the strengths of balanced and unbalanced motions vary geographically, the L_S value inferred along 165°E is spatially highly inhomogeneous. For example, although the balanced KE levels are both high in the Kuroshio Extension and Equatorial bands, weak unbalanced motion results in a small separation scale, $L_S = 8$km, in the Kuroshio Extension band. This L_S is much shorter than the regional baroclinic deformation radius $L_D = 30\sim40$km. In comparison, enhanced energy level by unbalanced motions and large baroclinic deformation radius ($L_D = 230$km) result in the separation scale $L_S = 200$km in the Equatorial band. In the STCC band with moderate levels of balanced and unbalanced motions, L_S has an intermediate value 15km and is shorter than the local baroclinic deformation radius ($L_D = 40\sim80$km).

The above L_S results are derived from the 40-100m velocity data. Since the ADCP measurements extend to below 100m, we present in Fig.4 eddy kinetic energy and its rotational and divergent components as a function of depth in each of the five bands. In the Kuroshio Extension and STCC bands, the rotational KE drop with depth is greater than the divergent KE drop; as a result, there is an overall tendency for L_S to lengthen with increasing depth (Figs.4c-4f). Dynamically, the drop in rotational KE is due to the weakening in baroclinic instability, and hence balanced eddy motions, with depth in these two bands. In the Equatorial band, $D3_L(r)$ remains largely unchanged in the 200m upper ocean. Much of the eddy variability in the Equatorial band, as shown in Fig.4i, is confined to this upper ocean layer. Below 200m, Fig.4j reveals that L_S shortens to ~100km in the 200~400m depth. This reduction in L_S is largely caused by the weakening of the wind-forced unbalanced motion beneath the Equatorial main thermocline (blue line in Fig.4i).

In the dynamically more stable NEC and WSG bands, balanced motions are subdued and the divergent KE has a 30-50% ratio over the rotational KE (Figs.4a and 4g). With this reduction in balanced motion, it is expected that L_S will increase. This indeed is the case for the NEC band where the observed L_S reaches 300km, exceeding the regional deformation radius ($L_D = 80\sim150$km). In the WSG band, on the other hand, an inverse cascade in a relatively narrow 10~50km window emerges as a surprise. Influenced by atmospheric storm-track forcing, the unbalanced motion in the WSG band is mostly induced by surface winds in contrast to the tropical NEC band where the unbalanced motion is largely tidally-driven. The impact of this different energy source on unbalanced motions is discernible in the vertical profiles shown in Figs.4a-b versus 4g-h. In the wind-forced WSG, for example, the divergent KE amplitude exhibits a sudden drop beneath 120m and, corresponding to this drop, the 10-50km signal with $D3_L(r) > 0$ disappears (Figs.4a-b). These results are consistent with the wind-forced near-inertial motions being confined to the surface mixed layer. This WSG feature of sudden drop in divergent KE is in sharp contrast to Fig.4g in which the NEC's divergent KE amplitude is shown to decrease gradually over the 600m upper ocean.

Compared to tidally-induced wave motions that propagate away from their generation sites, the wind-forced near-inertial motions are weakly dispersive and tend to remain locally trapped (Thomas and Arun 2020). These characteristics likely allow the wind-forced near-inertial motion

to interact and exchange energy with the background geostrophic flows present in the WSG (recall Fig.2a), leading to the observed inverse cascade in the 10~50km window. It is worth noting that an idealized model study by Gertz and Straub (2009) found that when stochastic wind forcing is added to the wind-driven gyre circulation, the wind-forced near-inertial motions are able to extract energy from the background circulation at intermediate wavelengths, while transferring energy back to the balanced gyre circulation at short wavelengths corresponding to their model's dissipation scale. It will be of interest for future studies to clarify if the 10~50km inverse cascade range detected in our study corresponds to the dissipation range in the WSG of the North Pacific Ocean.

Throughout this study, we have emphasized the interplay between balanced and unbalanced motions in determining the scale that separates the bi-directional energy cascades. Although the shipboard ADCP data used in our analyses are confined to the western Pacific, we expect many of the results to be relevant in other regions of the world ocean. Given that the separation scale detected in the subtropical and subarctic North Pacific is on O(10km), there is a clear need to explore the global distribution of L_S and its variability based on future satellite measurements that can observe the fine-scale SSH and surface current concurrently. In this regard, the Surface Water and Ocean Topography (SWOT) mission (Morrow et al. 2019) and the future Winds and Currents Mission (WaCM) (Rodriguez et al. 2019) will hold keys to our improved understanding of the ocean scale interactions and energy transfers. Finally, we have removed the time-mean flow from our analyses to ensure isotropy in the velocity field. How presence of the mean circulation can affect the directional KE cascade will be an important topic for future research.

Acknowledgments

We are grateful to the past and present captains and crews of *R/V Ryofu Maru* and *Keifu Maru*, and staff of the Marine Division, Japan Meteorological Agency, for their long-term observational efforts. We also thank Rob Scott and an anonymous reviewer for their constructive comments that have helped to improve an early version of the manuscript. B.Q. and S.C. acknowledge support from NASA OSTST mission (NNX17AH33G and 80NSSC21K1186). P.K. acknowledges support of CNRS (France), LabexMer (ANR-10-LABX-19-01) as well as of the NASA-CNES SWOT mission.

Data Availability Statement

The eddy kinetic energy data from global surface drifter program is available at https://www.aoml.noaa.gov/phod/gdp/mean_velocity.php. Japan meterological Agency maintains a website http://www.data.jma.go.jp/gmd/kaiyou/db/ vessel_obs/data-report/ html/ship/ship_e.php that includes the repeat shipboard ADCP data along 165°E.

References

Alford, M., MacKinnon, J., Simmons, H. & Nash, J. (2016). Near-inertial internal gravity waves in the ocean. *Ann. Rev. Mar. Sci*., **8**, 95-123.

Aluie, H., Hecht M. & Vallis G. (2018). Mapping the energy cascade in the North Atlantic Ocean: The coarse-graining approach. *J. Phys. Oceanogr*., **48**, 225-244.

Arbic, B., Polzin, K., Scott, R., Richman, J. & Shriver, J. (2013). On eddy viscosity, energy cascades, and the horizontal resolution of gridded satellite altimeter products. *J. Phys. Oceanogr.,* **43**, 283-300.

Balwada, D., LaCasce, J. & Speer, K. (2016). Scale-dependent distribution of kinetic energy from surface drifters in the Gulf of Mexico. *Geophys. Res. Lett*., **43**, 10,856-10,863.

Boccaletti, G., Ferrari, R. & Fox-Kemper, B. (2007). Mixed layer instabilities and restratification. *J. Phys. Oceanogr*., **37**, 2228-2250.

Bühler, O., Callies, J. & Ferrari, R. (2014). Wave-vortex decomposition of one-dimensional ship-track data. *J. Fluid Mech*., **756**, 1007-1026.

Callies, J. & Ferrari, R. (2013). Interpreting energy and tracer spectra of upper-ocean turbulence in the submesoscale range (1-200 km). *J. Phys. Oceanogr*., **43**, 2456-2474.

Callies, J., Ferrari, R., Klymak, J. & Gula, J. (2015). Seasonality in submesoscale turbulence. *Nature Commun*., **6**, 6862.

Capet, X., McWilliams, J., Molemaker, M. & Shchepetkin, A. (2008). Mesoscale to submesoscale transition in the California Current system. Part III: Energy balance and Flux. *J. Phys. Oceanogr.*, **38**, 2256-2269.

Chaigneau, A., Pizarro, O. & Rojas, W. (2008). Global climatology of near-inertial current characteristics from Lagrangian observations. *Geophys. Res. Lett*., **35**, L13603.

Chelton, D., Schlax, M. & Samelson, R. (2011). Global observations of nonlinear mesoscale eddies. *Prog. Oceanogr*., **91**, 167-216.

Chen, X., Qiu, B., Chen, S., Qi, Y. & Du, Y. (2015). Seasonal eddy kinetic energy modulations along the North Equatorial Countercurrent in the western Pacific. J. Geophys. Res., 120, 6351-6362.

Chereskin, T., Rocha, C., Gille, S., Menemenlis, D. & Passaro, M. (2019). Characterizing the transition from balanced to unbalanced motions in the southern California Current. *J. Geophys. Res.*, **124**, 2088-2109.

Cho, J.Y.N. & Lindborg, E. (2001). Horizontal velocity structure functions in the upper troposphere and lower stratosphere: 1. Observations. J. Geophys. Res., 106, 10223-10232.

Davidson, P. (2015). *Turbulence: An Introduction for Scientists and Engineers*. Oxford Univ. Press, 657 pp.

Favorite, F., Dodimead, A. & Nasu, K. (1976). Oceanography of the subarctic Pacific region, 1960-1971. Bull. Int. North Pacific Fish. Comm. 33, 1-187.

Ferrari, R. & Wunsch C. (2009). Ocean circulation kinetic energy: Reservoirs, sources, and sinks. *Annu. Rev. Fluid Mech*., **41**, 253-282.

Fox-Kemper, B., Ferrari, R. & Hallberg, R. (2008). Parameterization of mixed layer eddies. Part I: theory and diagnosis. *J. Phys. Oceanogr*., **38**, 1145-1165.

Fu, L.-L., Chelton, D.E., Le Traon, P.-Y. & Morrow, R. (2010). Eddy dynamics from satellite altimetry. *Oceanography*, **23**, 14-25.

Gertz, A. & Straub D.N. (2009). Near-inertial oscillations and the damping of midlatitude gyres: A modeling study. *J. Phys. Oceanogr*., **39**, 2338-2350.

Gille, S.T. & Llewellyn-Smith, S.G. (2000). Velocity probability density functions from altimetry. J. Phys. Oceanogr., 30, 125-136.

Held, I., Pierrehumbert, R., Garner, S. & Swanson, K. (1985). Surface quasi-geostrophic dynamics. *J. Fluid Mech*., **282**, 1-20.

Klein, P., Hua, B.L., Lapeyre, G., Capet, X., Le Gentil, S. & Sasaki, H. (2008). Upper ocean turbulence from high-resolution 3D simulations. *J. Phys. Oceanogr*., **38**, 1748-1763.

Kobashi, F. & Kawamura, H. (2002). Seasonal variation and instability nature of the North Pacific Subtropical Countercurrent and the Hawaiian Lee Countercurrent. J. Geophys. Res., 107, C03185.

Laurindo, L., Mariano, A. & Lumpkin, R. (2017). An improved near-surface velocity climatology for the global ocean from drifter observations. *Deep-Sea Res. I*, **124**, 73-92.

Lindborg, E. (2007). Horizontal wavenumber spectra of vertical vorticity and horizontal divergence in the upper troposphere and lower stratosphere. *J. Atmos. Sci*., **64**, 1017-1025.

Lindborg, E. (2015). A helmholtz decomposition of structure functions and spectra calculated from aircraft data. *J. Fluid Mech*., **762**, R4, doi:10.1017/jfm.2014.685.

Lindborg, E. & Cho J. (2001). Horizontal velocity structure functions in the upper troposphere and lower stratosphere II – Theoretical considerations. *J. Geophys. Res*., **106**, 10,233-10,241.

Morrow, R. & Co-authors (2019). Global observations of fine-scale ocean surface topography with the Surface Water and Ocean Topography (SWOT) mission. *Front. Mar. Sci*., **6**, 232. http://doi.org/10.3389/fmas.2019.00232.

Nakano, H., Tsujino, H., Sakamoto, K., Urakawa, S., Toyoda, T. & Yamanaka G. (2018). Identification of the fronts from the Kuroshio Extension to the Subarctic Current using absolute dynamic topographies in satellite altimetry products. *J. Oceanogr*., **74**, 393-420.

Philander, S. (1976). Instabilities of zonal equatorial currents. J. Geophys. Res., 81, 3725-3735.

Poje, A., Ozgokmen, T., Bogucki, D.& Kirwan, A. (2017). Evidence of a forward energy cascade and Kolmogorov self-similarity in submesoscale ocean surface drifter observations. *Physics of Fluids*, **29**(2), 020701.

Qiu, B. (1999). Seasonal eddy field modulation of the North Pacific Subtropical Countercurrent:

TOPEX/Poseidon observations and theory. J. Phys. Oceanogr., 29, 2471-2486.

Qiu B. & Chen S. (2005). Variability of the Kuroshio Extension jet, recirculation gyre, and mesoscale eddies on decadal time series. J. Phys. Oceanogr., 35, 2090-2103.

Qiu, B., Scott R. & Chen S. (2008). Length scales of eddy generation and nonlinear evolution of the seasonally-modulated South Pacific Subtropical Countercurrent *J. Phys. Oceanogr.*, **38**, 193-206.

Qiu, B., Chen, S., Klein, P., Sasaki, H. & Sasai, Y. (2014). Seasonal mesoscale and submesoscale eddy variability along the North Pacific SubtropicalCountercurrent. *J. Phys. Oceanogr*., **44**, 3079-3098.

Qiu, B., Nakano, T., Chen, S. & Klein, P. (2017). Submesoscale transition from geostrophic flows to internal waves in the northwestern Pacific upper ocean. *Nature Commun*., **8**, 14055.

Qiu, B., Chen, S., Klein, P., Wang, J., Torres, H., Fu, L.-L., & Menemenlis, D. (2018). Seasonality in transition scale from balanced to unbalanced motions in the World Ocean. *J. Phys. Oceanogr.*, **48**, 591-605.

Richards, K., Natarov, A., Firing, E., Kashino, Y., Soares, S., Ishizu, M., Carter, G., Lee, J. & Chang, K. (2015). Shear-generated turbulence in the equatorial Pacific produced by small vertical scale flow features. *J. Geophys. Res*., **120**, 3777-3791.

Richman, J., Arbic, B., Shriver, J., Metzger, E. & Wallcraft, A. (2012). Inferring dynamics from the wavenumber spectra of an eddying global ocean model with embedded tides. *J. Geophys. Res.*, **117**, C12012.

Rocha, C.B., Chereskin, T.K., Gille, S.T. & Menemenlis, D. (2016). Mesoscale to submesoscale wavenumber spectra in Drake Passage. J. *Phys. Oceanogr*., **46**, 601-620.

Rodriguez, E., & Co-authors (2019). The Winds and Currents Mission concept. *Front. Mar. Sci*., **6**, 438. http://doi.org/10.3389/fmas.2019.00438.

Sasaki, H., Klein, P., Qiu, B. & Sasai, Y. (2014). Impact of oceanic-scale interactions on the seasonal modulation of ocean dynamics by the atmosphere. *Nature Commun*., **5**, 5636.

Savage, A. & Co-authors (2017). Frequency content of sea surface height variability from internal gravity waves to mesoscale eddies, *J. Geophys. Res*., **122**, 2519-2538.

Schlösser, F. & Eden, C. (2007). Diagnosing the energy cascade in a model of the North Atlantic. *Geophys. Res. Lett*., **34**, L02604.

Scott, R. & Wang F. (2005). Direct evidence of an oceanic inverse kinetic energy cascade from satellite altimetry. *J. Phys. Oceanogr*., **45**, 1650-1666.

Sérazin, G., Marin, F., Gourdeau, L., Cravatte, S., Morrow, R. & Dabat, M.-L. (2020). Scale-dependent analysis of in situ observations in the mesoscale to submesoscale range around New Caledonia. *Ocean Sci*., **16**, 907-925.

Thomas, J. & Arun S. (2020). Near-inertial waves and geostrophic turbulence. *Phys. Rev. Fluids*, **5**, 014801.

Tulloch, R., Marshall, J., Hill, C. & Smith, S.S. (2011). Scales, growth rates, and spectral fluxes of baroclinic instability in the ocean. *J. Phys. Oceanogr*., **41**, 1057-1076.

Wang, S., Liu, Z. & Pang C. (2015). Geographical distribution and anisotropy of the inverse kinetic energy cascade, and its role in the eddy equilibrium processes. *J. Geophys. Res*., **120**, 4891-4906.

Waterman, S., Hogg, N., & Jayne, S. (2011). Eddy-mean flow interaction in the Kuroshio Extension region. J. Phys. Oceanogr., 41, 1182-1208.

Yang, Y. & Liang, X. (2016). The Instabilities and multiscale energetics underlying the mean interannual-eddy interactions in the Kuroshio Extension Region. J. Phys. Oceanogr. 46, 1477-1494.

Young, R.M.B., & Read, P.L. (2017). Forward and inverse kinetic energy cascades in Jupiter's turbulent weather layer. Nat. Physics, 13, DOI: 10.1038/NPHYS4227.

Zedler, S., Powell, B. Qiu, B. & Rudnick D. (2019). Energy transfer in the western tropical Pacific. *Oceanography*, **32** (4), 136-145.

Zhao, Z. & D'Asaro, E. (2011). A perfect focus of the internal tide from the Mariana Arc. *Geophys. Res. Lett*., **38**, L14609.

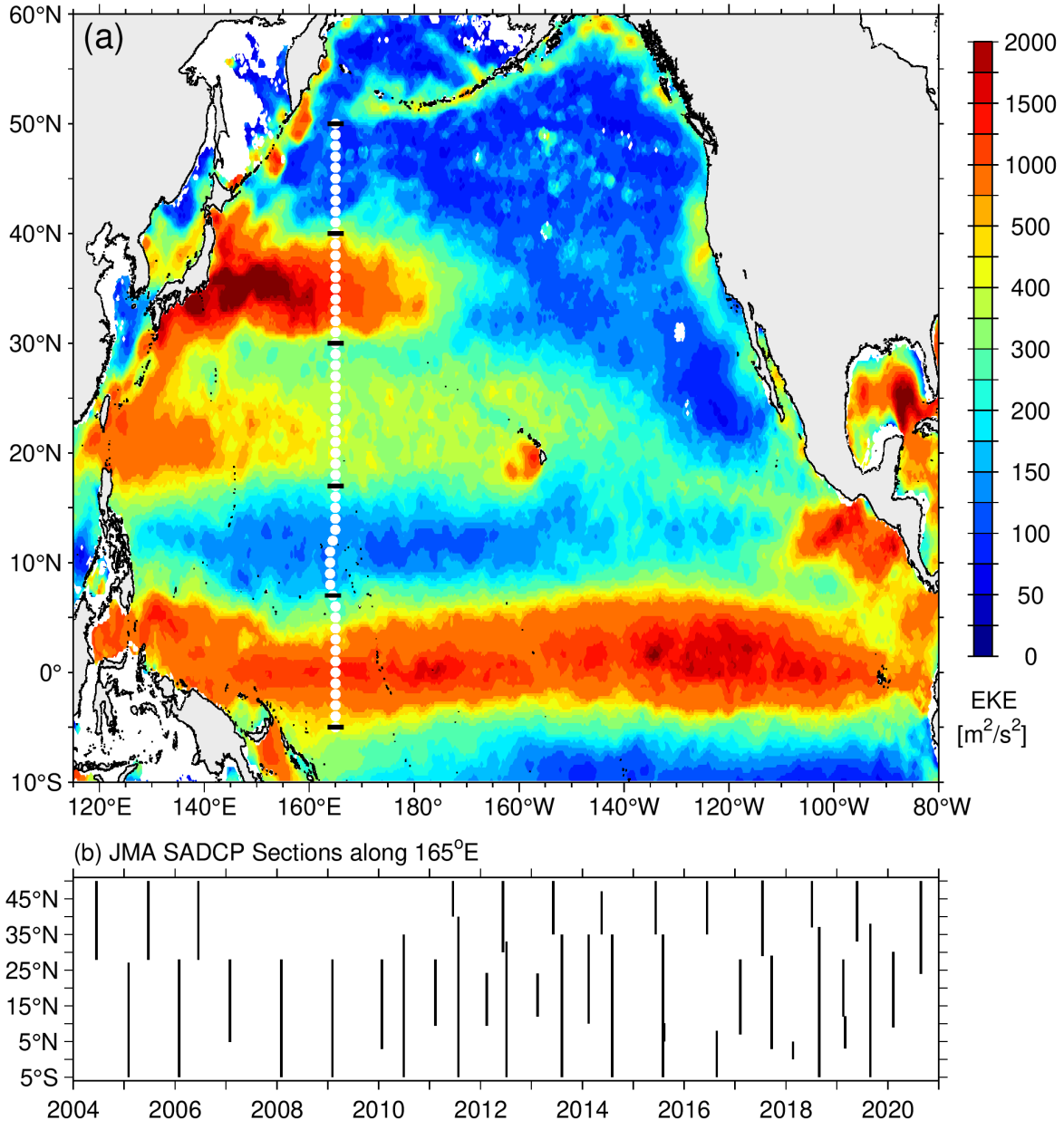

Figure 1. (a) Surface eddy kinetic energy distribution in the northwestern Pacific based on global surface drifter measurement (Laurindo et al. 2017). White dots along 165°E denote the track of shipboard ADCP measurements by JMA and short black lines along 40°N, 30°N and 17°N, and 7°N demarcate the boundaries of the Western Subarctic Gyre, the Kuroshio Extension, the Subtropical Countercurrent, the North Equatorial Current, and the Equatorial band. (b) Time-latitude plot of the 38 cruises used in the present study.

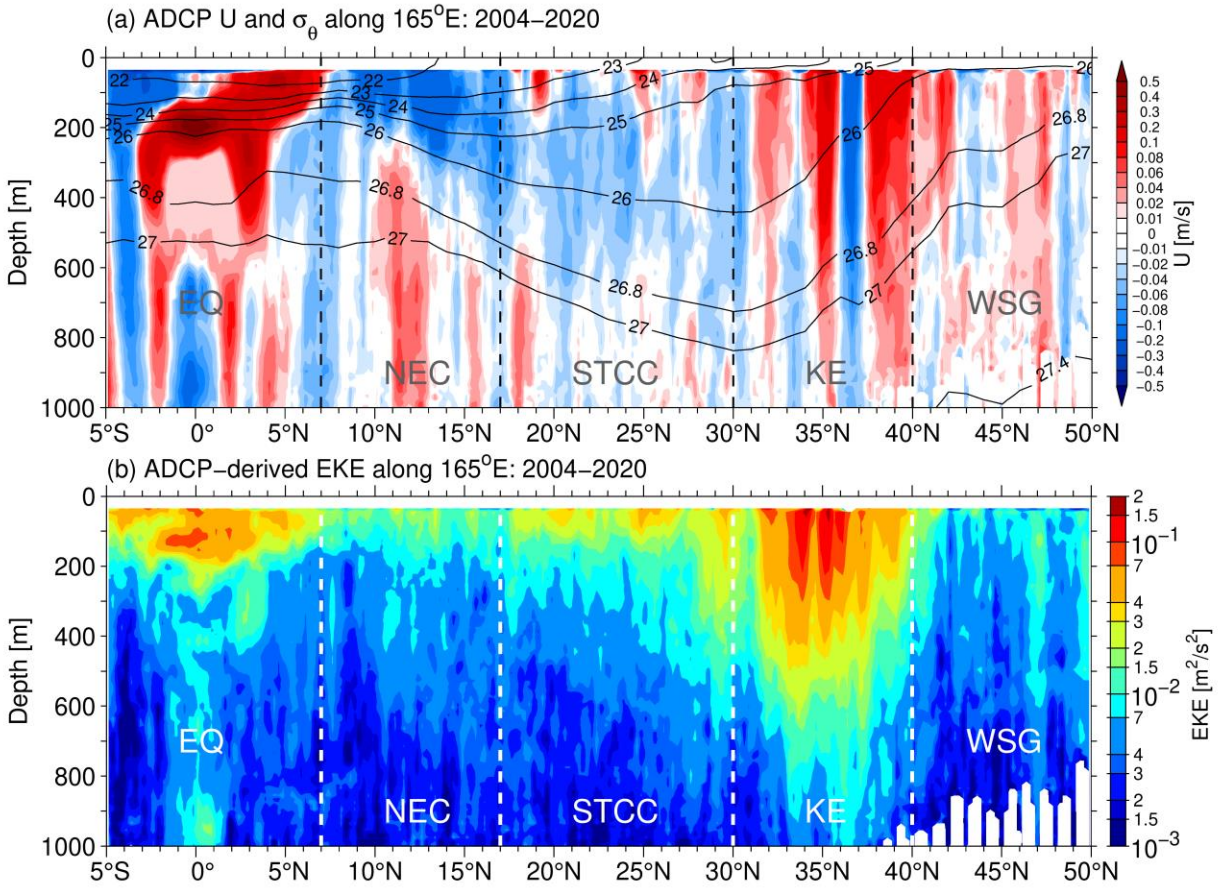

Figure 2. Latitude-depth sections of (a) ADCP-derived zonal mean velocity (colored contours) and CTD-derived density (black contours in σ_θ). Red (blue) colors denote eastward (westward) flows. (b) ADCP-derived eddy kinetic energy. Here, eddy velocities are evaluated by removing the time-mean velocities from individual cruises. Dashed lines delineate the dynamical bands used in the structure function analyses.

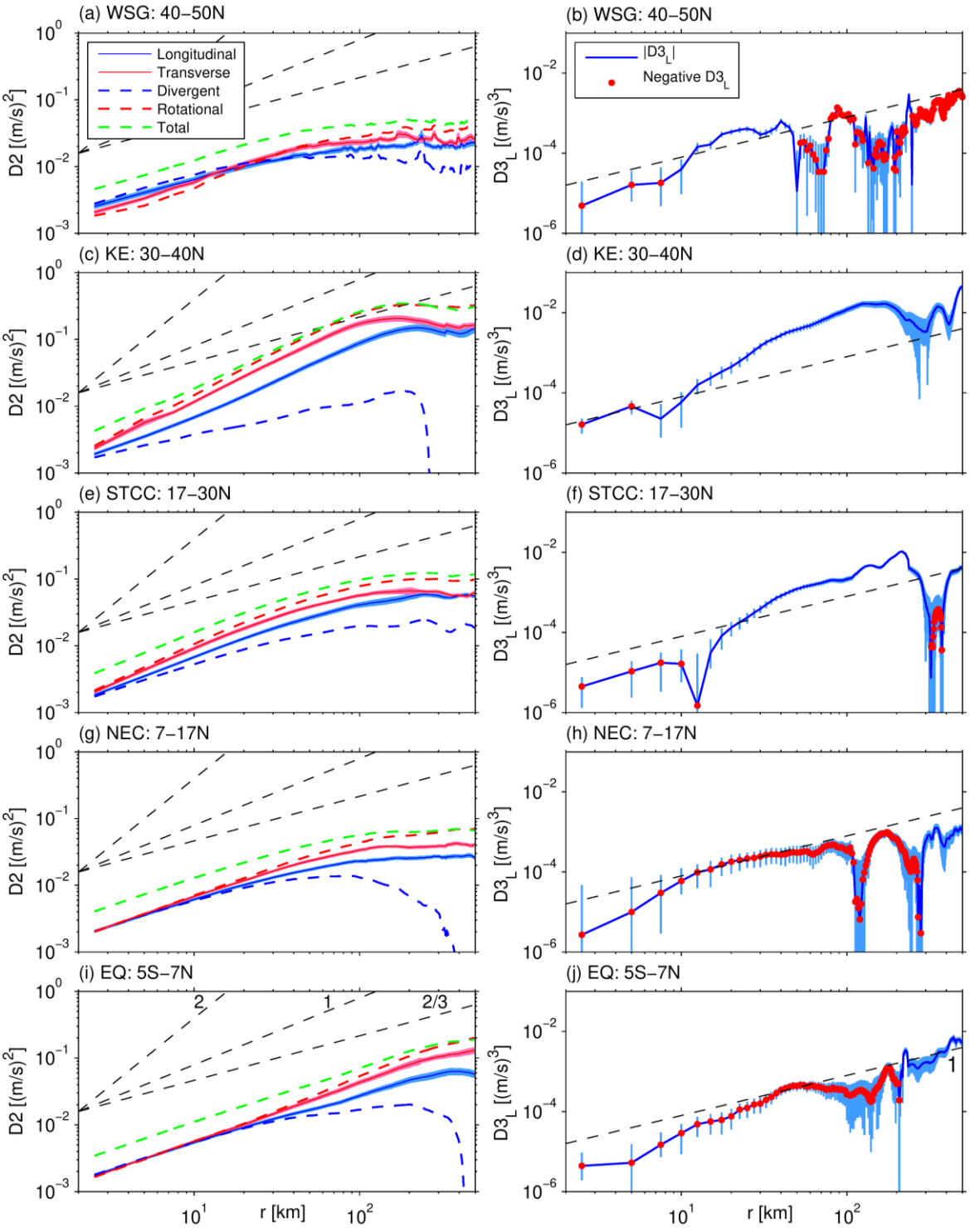

Figure 3. Left column: Different components of the second-order SFs in (a) WSG, (c) Kuroshio Extension, (e) STCC, (g) NEC, and (i) Equator bands. Straight dashed lines denote reference power laws of r^2, r^1, and $r^{2/3}$, respectively. Right column: Third-order SFs in the corresponding five bands. Negative values are marked by red circles and dashed line denotes reference power law of r^1. In all plots, vertical shades/bars represent standard error.

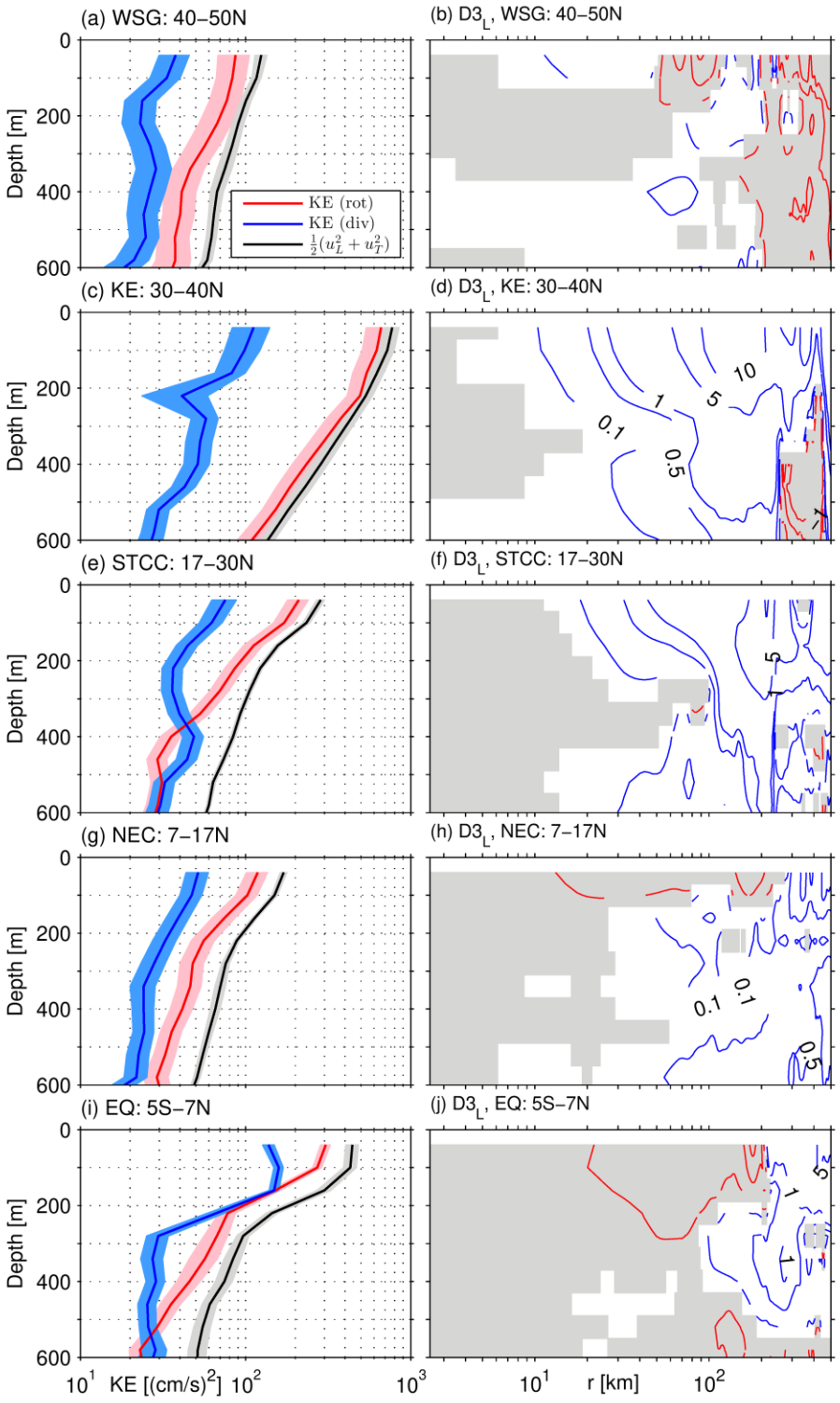

Figure 4. Left column: Eddy kinetic energy (black line) and its rotational (red) and divergent (blue) components as a function of depth in the five bands. Horizontal shades represent standard error. Right column: Third-order SF as a function of depth in the five bands. Negative values are marked by red contours with shading. Unit in 10^{-3} m^3/s^3.